Development of microfluidic platform capable of characterizing cytoplasmic viscosity, cytoplasmic conductivity and specific membrane capacitance of single cells

Yan Liu[1,2] · Ke Wang[3] · Xiaohao Sun[4] · Deyong Chen[1,2,5] · Junbo Wang[1,2,5] · Jian Chen[1,2,5]

Abstract

This paper presents a microfluidic platform capable of characterizing cytoplasmic viscosity μ_{cy}, cytoplasmic conductivity σ_{cy} and specific membrane capacitance C_{sm} of single cells continuously. A travelling cell is forced to squeeze through a major microfluidic constriction channel and aspirated into a side microfluidic constriction channel with cell aspiration length and impedance variations captured and translated into intrinsic markers of μ_{cy}, σ_{cy} and C_{sm} based on an equivalent biophysical model. As a demonstration, μ_{cy}, σ_{cy} and C_{sm} of hundreds of HL-60 cells that were native or treated by Cytochalasin D (CD for cytoskeleton modulation) or Concanavalin A (ConA for membrane regulation) were quantified where high success rates of cell type classification were found, which were 88.0% for HL-60 cells vs. HL-60 + CD cells and 75.6% for HL-60 cells vs. HL-60 + ConA cells. Furthermore, the microfluidic system was used to process granulocytes from two healthy donors where comparable distributions of μ_{cy}, σ_{cy} and C_{sm} and low success rates of cell type classification ($< 60\%$) were found, indicating that there may exist ranges of μ_{cy} (10–20 Pa•s), σ_{cy} (0.4–0.6 S/m) and C_{sm} (2.0–3.0 μF/cm^2) for normal granulocytes. In summary, the developed microfluidic system can collect cytoplasmic viscosity, cytoplasmic conductivity and specific membrane capacitance from hundreds of single cells simultaneously and may provide new perspective for future developments of hematology analyzers.

Keywords Microfluidics · Single-cell analysis · Multiple-parameter characterization · Crossing constriction channel · Concurrent measurement

1 Introduction

Biophysical properties of single cells mainly include biomechanical properties (e.g., membrane cortical tension, cytoplasmic viscosity, Young's modulus) and bioelectrical properties (e.g., membrane capacitance and cytoplasmic conductivity) (Zheng et al. 2013). Variations in single-cell biophysical properties have been closely correlated with

Yan Liu, Ke Wang and Xiaohao Sun co-first authors.

✉ Junbo Wang
jbwang@mail.ie.ac.cn

✉ Jian Chen
chenjian@mail.ie.ac.cn

1   State Key Laboratory of Transducer Technology, Aerospace Information Research Institute, Chinese Academy of Sciences, Beijing, China

2   School of Electronic, Electrical and Communication Engineering, University of Chinese Academy of Sciences, Beijing, China

3   School of Electronic Engineering, Beijing University of Posts and Telecommunications, Beijing, China

4   Department of Mechanical Engineering, University of Colorado Boulder, Boulder, USA

5   School of Future Technology, University of Chinese Academy of Sciences, Beijing, China

various biological processes, including (1) abnormalities of red and white blood cells (Yang et al. 2017; Liu et al. Feb 2018; Honrado et al. 2018; Guruprasad Feb 2019; Hassan, et al. 2017; Prieto 2016; Toepfner, et al. 2018; Bashant Jun 2019); (2) tumour cells in migration and evasion (Ahuja 2019; Ahmmed 2018; Che et al. 2017); and (3) stem cells in differentiation (Zhou et al. (2016); Xavier et al. 2017; Fan et al. 2019; Xavier 2016; Jacobi et al. 2019). Although these biophysical parameters are of importance, conventional characterization techniques (e.g., atomic force microscopy and electrorotation) suffer from limited throughputs and have difficulties in quantifying these biophysical properties simultaneously (e.g., ~10 cells per cell type based on atomic force microscopy (Cross et al. Dec 2007) and ~20 cells per cell type based on electrorotation (Becker et al. 1995).

Due to dimensional comparisons of microfluidics with biological cells, high-throughput quantification of single-cell biophysical properties have been realized by various microfluidic platforms (Xu et al. 2016; Liang et al. 2019; Darling and Carlo 2015; Wu 2018). For the characterization of single-cell mechanical properties, microfluidics-based deformability cytometry has been used for single-cell mechanical property characterization, where single cells travel rapidly in microfluidic channels and show deformations in response to geometrical constrictions and/or fluid stresses (Deng et al. 2017; Leblanc-Hotte 2019; Reichel et al. 2019). Based on equivalent biomechanical models, these raw data of cell deformations can be interpreted into intrinsic single-cell biomechanical markers including Young's modulus and cytoplasmic viscosity (Rosendahl 2018; Kang Mar 2019; Armistead et al. 2019; Fregin, et al. 2019; Nyberg et al. 2017; Davidson 2019; Wang et al. 2019). Meanwhile, for the characterization of single-cell electrical properties, microfluidics-based impedance flow cytometry has also been used where single cells under measurements travel rapidly through microfluidic channels with impedance signals sampled (Jaffe and Voldman 2018; Ninno, et al. 2019; Feng et al. 2019; Yang and Ai 2019; Serhatlioglu et al. 2019; Reale et al. 2019; Wang et al. 2017). Based on equivalent bioelectrical models, these raw impedance data can be translated into intrinsic single-cell bioelectrical markers including specific membrane capacitance and cytoplasmic conductivity (Zhao 2018; Zhang 2019). Based on these approaches, although large populations of single-cell biophysical properties were reported, they can only characterize biomechanical or bioelectrical properties, not both and thus their performances in cell type classification and cell status evaluation were limited.

Compared with the quantification of biomechanical or bioelectrical parameters only, simultaneous quantifications of both types of biophysical parameters can definitely provide more insights in cell analysis (Zheng et al. 2013). Recently, high-throughput single-cell characterization of

biomechanical and bioelectrical properties has been realized by combining deformability and impedance microfluidic flow cytometry where single cells are forced to deform through microfabricated constriction channels (with cross-sectional areas smaller than cells) continuously with corresponding images captured and impedance recorded, enabling high-rate classifications of wild and modified breast cancer cells of MCF-7 (Yang et al. 2019; Zhou et al. 2018), breast cancer cells of MDA-MB-231 and normal epithelial cells of MCF-10A (Ren et al. Jul (2019)), breast cancer cells of H460, H446, A549, 95D and 95C Wang (2017) and malaria-infected red blood cells (Yang et al. 2017). Although powerful, the majority of these previously reported approaches can only collect raw biophysical markers (e.g., transit times and impedance variations during cell travelling through constrictions) rather than intrinsic biophysical markers (e.g., cytoplasmic viscosity and membrane capacitance) due to the lack of sensing structures and equivalent models, leading to compromised performances in cell type classification.

To address this issue, this paper presents a microfluidic system with crossing constriction channels capable of characterizing intrinsic biophysical markers of single cells (e.g., cytoplasmic viscosity, cytoplasmic conductivity and specific membrane capacitance) continuously. A crossing constriction channel is composed of a major constriction channel for cell deformation and travelling while perpendicularly positioned side constriction channels were used for deformation and impedance measurements of single cells. Based on an equivalent biophysical model for cell travelling at the junction of the major and side constriction channels, these raw biophysical parameters were translated into intrinsic biophysical markers of cytoplasmic viscosity, cytoplasmic conductivity and specific membrane capacitance. In comparison to previous approaches of high-throughput quantifying single-cell biomechanical or bioelectrical markers only, the simultaneous quantifications of both biomechanical and bioelectrical properties of single cells by this approach can significantly improve the success rates of cell type classification.

2 Materials and methods

2.1 Materials

Unless otherwise indicated, all reagents for cell culture and treatments were purchased from Life Technologies Corporation (USA). The HL-60 cell line and the corresponding culture medium (RPMI 1640, w/o Hepes) were purchased from National Infrastructure of Cell Line Resources (China). Granulocytes were isolated from blood samples of healthy donors based on gradient density centrifugation enabled by Percoll (GE Healthcare, USA). Materials required for device

fabrication included SU-8 photoresist (MicroChem Corporation, USA), AZ serial photoresist (AZ Electronic Materials Corporation, USA) and 184 silicone elastomer (Dow Corning Corporation, USA).

2.2 Working flowchart

Figure 1 shows the working flowchart for the microfluidic platform for simultaneous quantifications of single-cell cytoplasmic viscosity, cytoplasmic conductivity and specific membrane capacitance. There are mainly three steps of cell preparation, device operation, data processing and analysis. In cell preparation, HL-60 cells and granulocytes were prepared individually. For HL-60 cells, they were treated with CD to modulate cytoskeleton or ConA to modulate membrane properties. As to granulocytes, they were separated from whole blood samples of healthy donors based on gradient density centrifugation (see Fig. 1a).

In device operation, suspended blood cells were forced to deform through the major constriction channel continuously and invade into the side constriction channel when travelling through the junction of the major and the side constriction channels. During this process, the cell images as a function of time were recorded by an inverted microscope in connection with a high-speed camera while impedance amplitudes and phases were sampled by a lock-in amplifier (see Fig. 1b).

In data processing and analysis, the cell aspiration length L_p, an indicator of cell invading into the side constriction channel was obtained based on image processing and fitted by an empirical model, enabling the extraction of the size-independent intrinsic biophysical marker of μ_{cy}. Experimental results of preliminary impedance data were translated into size-independent intrinsic bioelectrical markers of σ_{cy} and C_{sm}, based on an equivalent theoretical model. Neural network-based pattern recognition was used
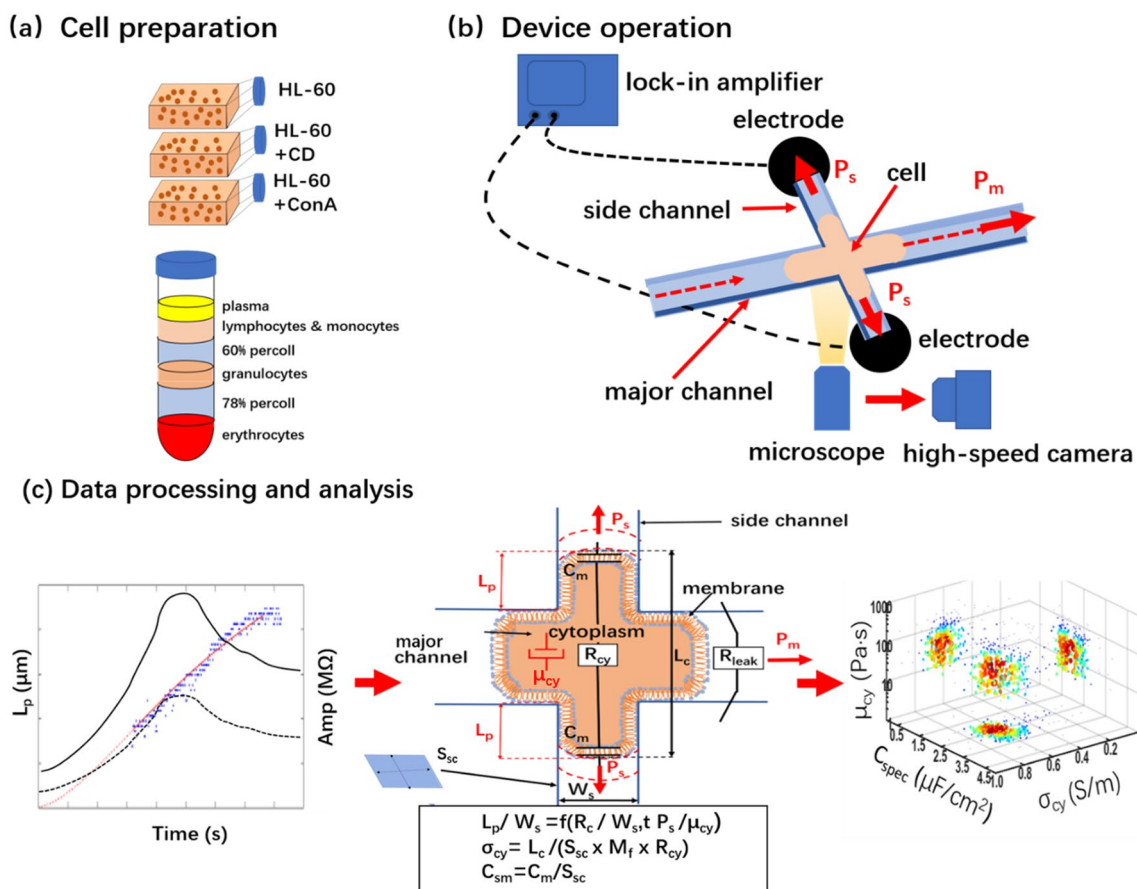
Fig. 1 Schematics for the microfluidic platform capable of characterizing single-cell cytoplasmic viscosity μ_{cy}, cytoplasmic conductivity σ_{cy} and specific membrane capacitance C_{sm}, simultaneously, which mainly included key steps of **a** cell preparation, **b** device operation, **c** data processing and analysis. In operations, a travelling cell is forced to squeeze through the major constriction channel and aspirated into the side constriction channel with cell aspiration length captured by a high-speed camera and corresponding impedance variations monitored by a lock-in amplifier. Based on the equivalent mechanical and electrical model of a travelling cell at the junction of the major and the side constriction channels, these preliminary biophysical data were translated into intrinsic biophysical markers of cytoplasmic viscosity, cytoplasmic conductivity and specific membrane capacitance

to conduct cell-type classification based on μ_{cy}, σ_{cy}, C_{sm} individually or in combination (see Fig. 1c).

2.3 Cell preperation

HL-60 cells were cultured in suspension with RPMI-1640 medium plus 20% fetal bovine serum. For cell treatments, native HL-60 cells were incubated with 1 µg/mL CD or 10 µg/mL ConA for 30 min, respectively. Before experiments, the concentration of HL-60 cells was adjusted to $\sim 5 \times 10^6$ cells per mL based on centrifugation and resuspension.

As for normal granulocytes, they were separated from peripheral blood samples of two healthy donors based on density centrifugation. More specifically, solutions of 78% Percoll, 60% Percoll and the whole blood samples were centrifuged at 400 g for 30 min. Then, the layer of granulocytes was collected and resuspended in RPMI-1640 medium at a concentration of 10^7 cells per mL for the following experiments.

2.4 Device design, fabrication, and operation

The crossing constriction channel developed in this study consists mainly of a major constriction channel and a side constriction channel with rectangular cross-sections. A single cell to be measured needs to be squeezed into the major constriction channel and tightly sealed with the channel walls. Thus, a slightly smaller cross-sectional area should be used for the major constriction channel, comparing to that of the cell under measurement. Based on diameter ranges of the adopted HL-60 cells (i.e., 10–12 µm) and granulocytes from human samples (i.e., 8–10 µm), the geometries of the major constriction channels were chosen as 6 µm in width × 4 µm in depth for HL-60 and 4 µm in width × 4 µm in depth for granulocytes, respectively.

As the deformed cell flows through the crossing point of the major and the side constriction channels, the cytoplasm is partially aspirated into the side channel due to the negative pressure. As to the cross-section dimensions of the side channel, they should be as small as possible to avoid fluid leakage at the corners between the cell and channel walls. However, to decrease the basal impedance without travelling cells, the dimensions should be as large as possible. After a trade-off process, the cross-section dimensions of the side constriction channel were selected as 3 µm in width × 4 µm in depth for HL-60 cells and 2 µm in width × 4 µm in depth for granulocytes, respectively.

The device fabrication was conducted based on conventional microfabrication techniques, which mainly focused on the replication of PDMS-based two-layer crossing constriction channels from a mould master made of silicon at bottom and SU-8 on top, respectively. The key fabrication steps included the formation of the silicon-based layer of crossing constriction channels using deep reactive ion etching, the formation of the SU-8 based second layer using photolithography, the formation of PDMS-based crossing constriction channels using soft lithography, the formation of the glass slide layer with patterned electrodes based on lift-off technologies and bonding between the PDMS layer and the metal patterned glass layer.

In device operation, the microfluidic device was first fully filled with culture medium, followed by the addition of cell suspensions. Negative pressures of 5 kPa and 3 kPa generated from two pressure calibrators (DIP-610 and PACE 5000 pressure calibrators, Druck, UK) were applied on the exit end of the major constriction channel and the two ends of the side constriction channel, respectively, so that cells were forced to travel through the major constriction channel and deform into the side constriction channel. Images of the deformed cell were captured by a high-speed camera (M320S, Phantom, USA) which was connected with an inverted microscope (IX71, Olympus, Japan) at a speed of 1000 frames per second. A two-frequency sinusoidal voltage signal (100 kHz + 250 kHz) was generated by a lock-in amplifier (model 7270 DSP lock-in amplifier, Signal Recovery, USA) and applied on the two ends of the side channel to monitor impedance profiles of the travelling single cell.

2.5 Data processing

To measure L_p as a function of time for each cell tested, a sequence of image processing steps, including frame differencing, thresholding, particle removal using erosion, and edge detection were applied to the images acquired during experiments. Then, L_p was translated into intrinsic biomechanical parameter of μ_{cy} using a numerical model modified from the previous study (Wang et al. 2019) (see Fig. 1c). More specifically, a numerical relation between cytoplasmic viscosity μ_{cy} and aspiration pressure at the two ends of the side constriction channel P_s, equivalent side channel width W_s, cell radius R_c, aspiration length L_p as a function of time t was obtained based on finite element simulations. This relationship was further represented in a dimensionless format as $L_p/W_s = f(R_c/W_s, t \times P_s/\mu_{cy})$ where f is a nonlinear function obtained from simulations. This format was further used to fit experimental data of L_p as a function of time through nonlinear curve fitting with μ_{cy} as the fitting parameter, from which the cytoplasmic viscosity of single cells cell can be obtained.

The measured impedance data with amplitude and phase at 100 kHz (amp@100 kHz and phase@100 kHz) and 250 kHz (amp@250 kHz and phase@250 kHz) were translated into intrinsic bioelectrical parameters of σ_{cy} and C_{sm} using a theoretical model modified from the previous study (Zhang 2019) (see Fig. 1c). Briefly, impedance values

for individual cells at 100 and 250 kHz were processed to R_{leak} (an indicator of sealing properties of deformed cells with the walls of the side constriction channel), membrane capacitances C_m and cytoplasm resistances R_{cy}. Then, R_{cy} was translated into σ_{cy} based on the format of $\sigma_{cy} = L_c/(S_{SC} \times M_f \times R_{cy})$ where L_c represents cell elongation length at the crossing point, S_{SC} represents cross-sectional area of the side constriction channel and M_f represents a modification factor due to divergence of electrical lines at the crossing point. Meanwhile, C_m was further translated into C_{sm} based on the format of $C_{\text{sm}} = C_m/S_{sc}$.

In this study, the measurements of multiple samples were conducted with results summarized in scatter plots, box plots and distribution plots. More specifically, scatter plots use the method of drawing scatter points to represent the data distribution range and aggregation. Box plots use the minimum, first quartile, median, third quartile, and maximum values in a set of data to reflect the center position and spread of the data distribution. Distribution plots show the probability distribution of the data in different value intervals.

In addition, neural network based on pattern recognition was conducted to classify cell types where a two-layer (hidden and output layer) feed forward neural network with sigmoid hidden and softmax output neurons as well as a backpropagation algorithm was used (MATLAB 2016, MathWorks Corporation, USA). In this study, for the classification of two cell types (HL-60 vs. HL-60+CD or HL-60 vs. HL-60+ConA), the values of cytoplasmic viscosity, cytoplasmic conductivity and/or specific membrane capacitance were used as inputting datasets and the corresponding 0/1 matrices (0 represents HL-60 and 1 represents HL-60+CD or HL-60+ConA) were used as output matrices. The complete dataset made of a specific inputting dataset and a corresponding output matrix was divided into a 70% training data used by the network for its adjustment based on generated errors, a 15% validation data used to evaluate the generalization of the network, and a 15% testing data used to independently quantify the performance of the network after training and validation. As to the results, the neural network-based pattern recognition generated a confusion matrix where the orange, green and blue squares represent incorrect responses, correct responses, and the overall accuracies. More specifically, the successful classification rate of classifying two types of cells can be found in the lower right blue square with green color.

3 Results and discussion

With the development of microfluidics, a variety of microfluidic structures have been proposed for single-cell biophysical property characterization (Xu et al. 2016; Liang et al. 2019; Darling and Carlo 2015; Wu 2018). Among these sensing structures, crossing constriction channels have been recently used for single-cell biomechanical or bioelectrical property characterization.

More specifically, when the exit end of the major constriction channel and two ends of the side constriction channel were applied with negative pressures, travelling single cells were aspirated through the major constriction channel from inlet and when they reached the junction of the major and side constriction channels, cells deformed into side constriction channels partially. This deformation process was captured and translated into cytoplasmic viscosity based on the corresponding biomechanical model (Wang et al. 2019).

Meanwhile, when the exit end of the major constriction channel was applied with a negative pressure and two ends of the side constriction channel were sealed from environmental pressures but connected with an impedance analyzer, single cells were aspirated through the major constriction channel from inlet and when they reached the junction of the major and side constriction channels, cells sealed rather than invaded into the side constriction channel, leading to blocked electric lines and varied impedance data. These impedance variations were sampled and translated into cytoplasmic conductivity and specific membrane capacitance based on the corresponding bioelectrical model (Zhang 2019).

This study was aimed to characterize both biomechanical and bioelectrical properties of single cells leveraging the crossing constriction channel by addressing the conflicting point that previously cells were forced to aspirate into the side constriction for mechanical property characterization and seal rather than invade into the side constriction for electrical property characterization. To deal with this issue, in this study, negative pressures were applied on the exit end of the major constriction channel and the two ends of the side constriction channel, respectively, so that cells deformed into the side constriction channel with image captured and translated into cytoplasmic viscosity. Meanwhile, a lock-in amplifier was applied on the two ends of the side channel to monitor impedance profiles of the travelling single cell invading into the side constriction channel while both images and impedance profiles were used for the interpretation of cytoplasmic conductivity and specific membrane capacitance.

Figure 2 shows microscopic pictures of a HL-60 cell (a, b, c), a CD-treated HL-60 cell (e, f, g), a ConA-treated HL-60 cell (I, j, k) and a granulocyte from a healthy donor (m, n, o), travelling in the major constriction channel and deforming into the side constriction channel. Experimentally measured aspiration lengths, two-frequency amplitude and phase profiles as a function of time for these four representative cells are shown in d, h, l and p. The red lines and the crossing labels show the results of curve fitting and the location of the maximal impedance amplitudes, which were further used for
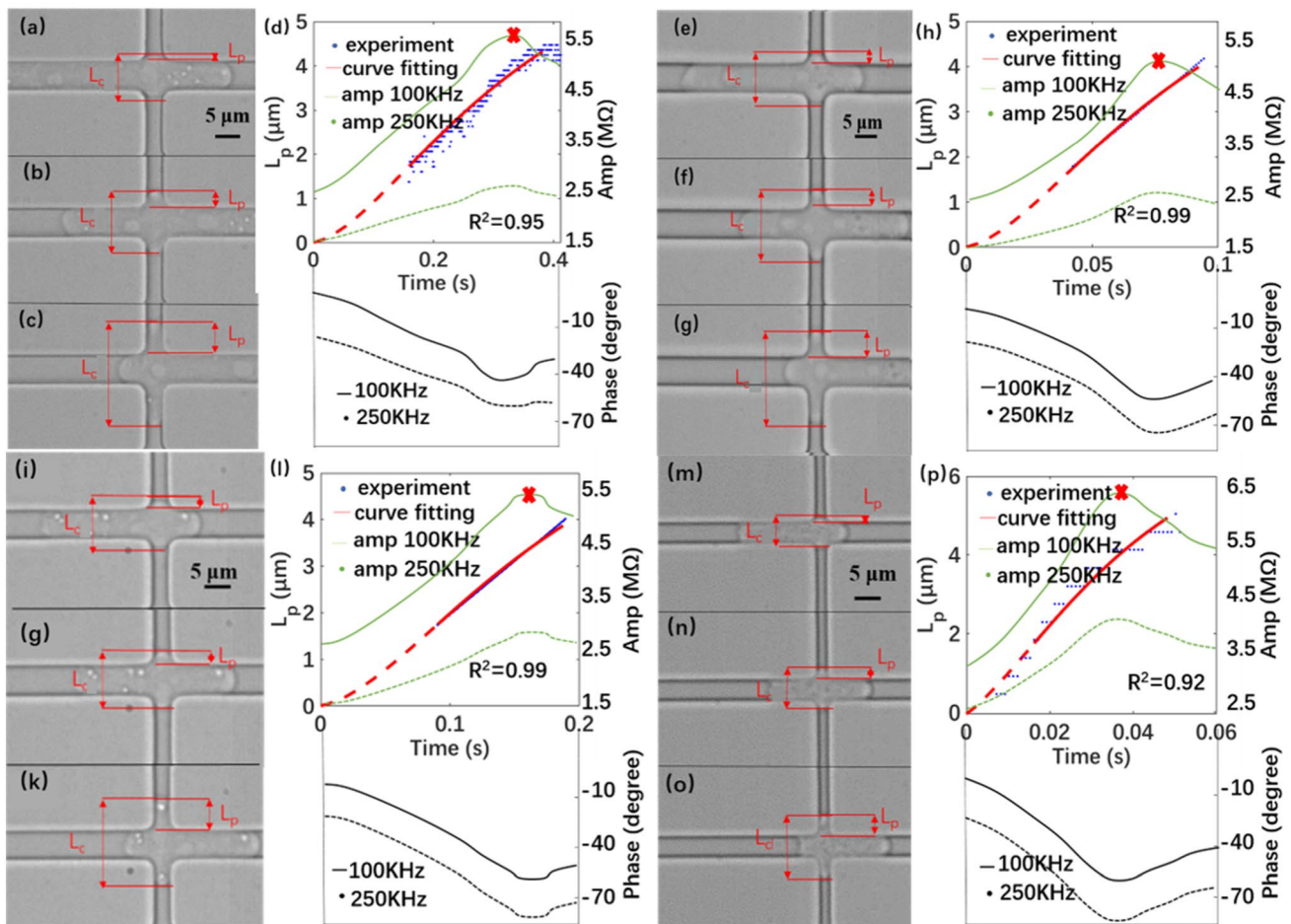
Fig. 2 Microscopic pictures of a HL-60 cell (**a**, **b**, **c**), a CD-treated HL-60 cell (**e**, **f**, **g**), a ConA-treated HL-60 cell (**i**, **j**, **k**) and a granulocyte from healthy donor I (**m**, **n**, **o**) travelling in the major constriction channel and deforming into the side constriction channel. Experimentally measured aspiration lengths, two-frequency amplitude and phase profiles as a function of time for these four representative cells are shown in (**d**, **h**, **l** and **p**). The red lines and the crossing labels show the results of curve fitting and the position of the maximal impedance amplitudes, which were further used for single-cell mechanical and electrical property characterization. Note that R^2 represents the degree of fitting of the regression curve to the experimental data where the closer the value of R^2 is to 1, the better the degree of fitting

single-cell mechanical and electrical property characterization, respectively.

Based on raw image and impedance data shown in Fig. 2, the processing durations for single cells travelling through the crossing constriction channel were in the ranges of ~ 0.1 s and thus the throughput of this microfluidic platform was roughly ~ 1 cell per second. In this study, when HL-60 cells with diameters of 10–12 μm and granulocytes from human samples with diameters of 8–10 μm were characterized by this microfluidic platform, the blockage of the major constriction channel was not often noticed. As to the blockage of the side constriction channel, this was not a concern since assymmetries of aspiration length in the two side constriction channels were seldom located. Currently, the bottleneck of this microfluidic platform is the high-speed camera which was used to record images of cell aspiration in the crossing constriction channel. In operations, the high-speed camera had to record images for several minutes with its internal memory fully occupied and then a few more minutes were required to transfer data from the high-speed camera to a computer. Due to this limitation, the high-speed camera cannot work continuously and thus it took roughly half an hour to collect both impedance and image data from hundreds of single cells.

Figure 3(a, b, c) shows scatter plots of μ_{cy} vs. R_c, box and distribution plots of μ_{cy} for HL-60 cells, CD-treated HL-60 cells and ConA-treated HL-60 cells. Specifically, three quartile values and peaking ranges of μ_{cy} of HL-60 cells under different conditions were quantified as 21.5 Pa•s, 40.4 Pa•s, 63.8 Pa•s and 42.9–68.7 Pa•s ($n_{cell} = 329$, HL-60), 14.8 Pa•s, 27.2 Pa•s, 58.8 Pa•s and 16.8–26.8 Pa•s
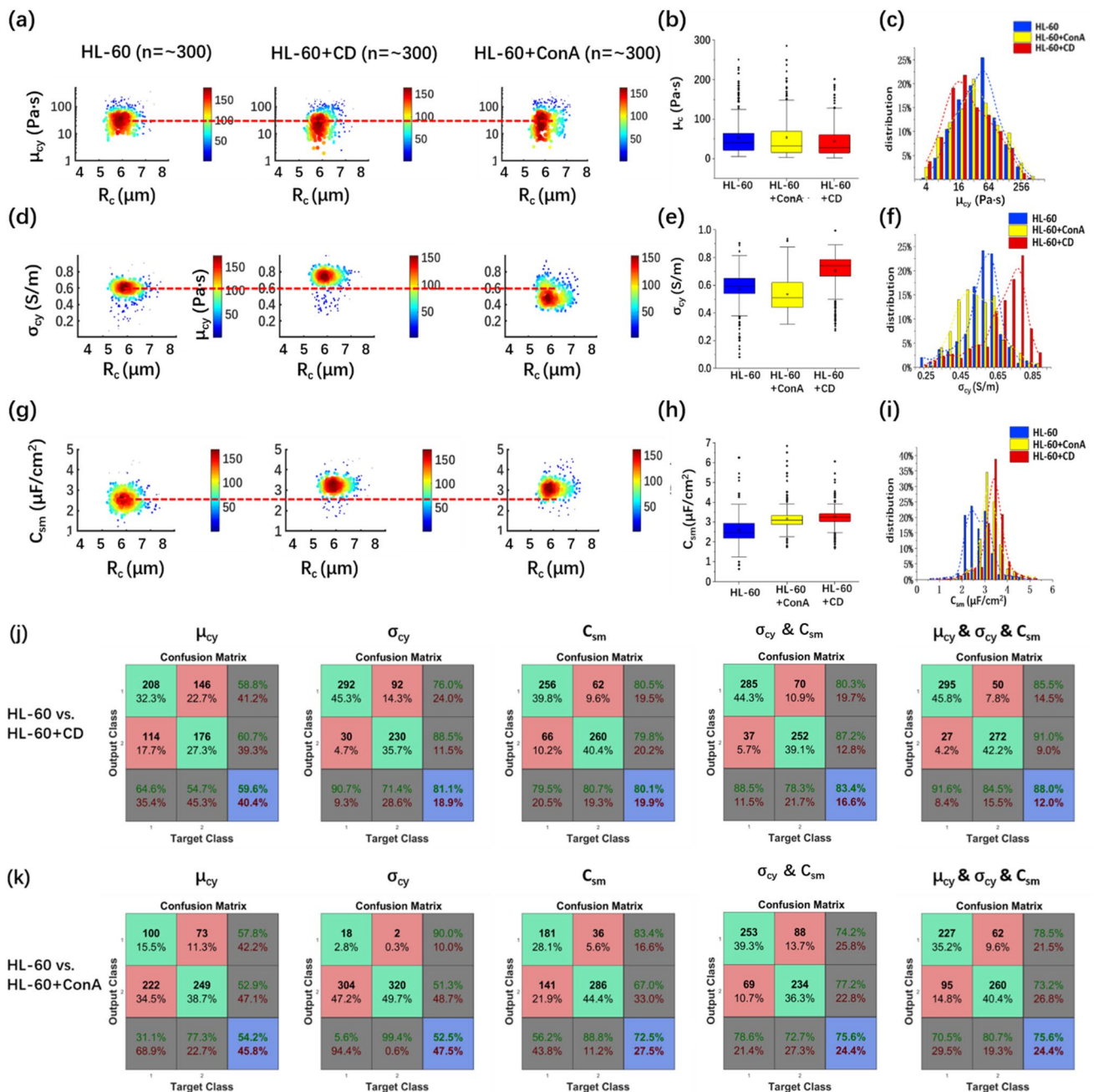
Fig. 3 **a**, **b**, **c**: Scatter plots of μ_{cy} vs. R_c (**a**), box (**b**) and distribution plots (**c**) of μ_{cy} for HL-60 cells, CD-treated HL-60 cells, and ConA-treated HL-60 cells. **d**, **e**, **f**: Scatter plots of σ_{cy} vs. R_c (**d**), box (**e**) and distribution plots (**f**) of σ_{cy} for HL-60 cells, CD-treated HL-60 cells, and ConA-treated HL-60 cells. **g**, **h**, **i**: Scatter plots of C_{sm} vs. R_c (**g**),

box (**h**) and distribution plots (**i**) of C_{sm} for HL-60 cells, CD-treated HL-60 cells, and ConA-treated HL-60 cells. Confusion matrix for the classifications of HL-60 cells vs. CD-treated HL-60 cells (**j**) and HL-60 cells vs. ConA-treated HL-60 cells (**k**) based on single-cell parameters of μ_{cy}, σ_{cy}, C_{sm}, σ_{cy} and C_{sm} and μ_{cy} and σ_{cy} and C_{sm}

($n_{cell} = 320$, HL-60 + CD), 15.8 Pa•s, 32.0 Pa•s, 70.1 Pa•s and 26.8–42.9 Pa•s ($n_{cell} = 320$, HL-60 + ConA).

The quantified values of μ_{cy} for HL-60 cells fell into the previously reported ranges (~ tens of Pa•s) (Wang et al. 2019) where only biomechanical parameter of μ_{cy} was measured, suggesting that electrical phenotyping of cells has no significant effects on cellular mechanical properties. HL-60

cells with the CD treatment indicated lower values of μ_{cy} in comparison to HL-60 cells (27.2 Pa•s Vs. 40.4 Pa•s), which agreed with the assumption that the treatment of cells with CD can compromise cytoskeletons. Neural network-based pattern recognition was conducted to classify HL-60 cells vs. HL-60 + CD cells based on μ_{cy}, producing a success rate of 59.6% (see Fig. 3(j)). These results indicate that although

μ_{cy} can be used to differentiate HL-60 cells with and without the treatment of CD, the only use of μ_{cy} can only provide limited insights in cell type classification.

Meanwhile, although HL-60 cells with the ConA treatment indicated marginally lower values of μ_{cy} in comparison to HL-60 cells (32.0 Pa•s Vs. 40.4 Pa•s), since a low success rate of 54.2% was obtained to classify HL-60 cells vs. HL-60 + ConA cells (see Fig. 3k), it is concluded that μ_{cy} is insensitive to the ConA treatment of cells, since ConA only binds with glycoproteins at the membrane domain and has limited effects on the cytoplasmic domains of cells.

Figure 3(d, e, f) shows scatter plots of σ_{cy} vs. R_c, box and distribution plots of σ_{cy} for HL-60 cells, CD-treated HL-60 cells, and ConA-treated HL-60 cells. Specifically, three quartile values and peaking ranges of σ_{cy} of HL-60 cells under different conditions were quantified as 0.54 S/m, 0.60 S/m, 0.65 S/m and 0.55–0.60 S/m ($n_{cell} = 329$, HL-60), 0.67 S/m, 0.74 S/m, 0.78 S/m and 0.70–0.75 S/m ($n_{cell} = 320$, HL-60 + CD), 0.44 S/m, 0.50 S/m, 0.62 S/m and 0.45–0.50 S/m ($n_{cell} = 320$, HL-60 + ConA).

The quantified values of σ_{cy} for HL-60 cells in this study fell into the previously reported ranges (~ 1 S/m (Wang 2017)) for single-cell electrical property characterization, suggesting that the simultaneous mechanical phenotyping of cells has no significant effects on electrical properties of cytoplasm. HL-60 cells with the CD treatment indicated higher values of σ_{cy} in comparison to HL-60 cells (0.74 S/m Vs. 0.60 S/m), which may again result from cytoskeleton compromise. Neural network-based pattern recognition was conducted to classify HL-60 cells vs. HL-60 + CD cells based on σ_{cy}, producing a success rate of 81.1% (see Fig. 3j). These results indicate that σ_{cy} can function as an effective parameter in classifying HL-60 cells and HL-60 + CD cells.

Meanwhile, HL-60 cells with ConA treatment indicated marginally lower values of σ_{cy} in comparison to HL-60 cells (0.50 S/m vs. 0.60 S/m) and neural network-based pattern recognition produced a low success rate of 52.5% when these two cell types were classified. These results again indicate that σ_{cy} is insensitive to the ConA treatment of cells, since ConA only binds with glycoproteins at the membrane domain and has limited effects on the cytoplasmic domains of cells.

Figure 3(g, h, i) shows scatter plots of C_{sm} vs. R_c, box and distribution plots of C_{sm} for HL-60 cells, CD-treated HL-60 cells, and ConA-treated HL-60 cells. Specifically, three quartile values and peaking ranges of C_{sm} of HL-60 cells under different conditions were quantified as 2.19 μF/cm^2, 2.46 μF/cm^2, 2.94 μF/cm^2 and 2.20–2.50 μF/cm^2 ($n_{cell} = 329$, HL-60), 3.03 μF/cm^2, 3.24 μF/cm^2, 3.42 μF/cm^2 and 3.10–3.40 μF/cm^2 ($n_{cell} = 320$, HL-60 + CD), 2.88 μF/cm^2, 3.09 μF/cm^2, 3.34 μF/cm^2 and 2.80–3.10 μF/cm^2 ($n_{cell} = 320$, HL-60 + ConA).

The quantified values of C_{sm} for HL-60 cells in this study fell into the previously reported ranges (~ 1 μF/cm^2 (Wang 2017)) for single-cell electrical property characterization, suggesting that the simultaneous mechanical phenotyping of cells has no significant effects on electrical properties of cell membranes. HL-60 cells with both CD and ConA treatments indicated higher values of C_{sm} in comparison to HL-60 cells (3.24 μF/cm^2 vs. 3.09 μF/cm^2 vs. 2.46 μF/cm^2), which may result from the fact that both the treatments of CD and ConA can affect membrane properties of single cells. Neural network-based pattern recognition produced success rates of 80.1% for HL-60 cells vs. HL-60 + CD cells and 72.5% for HL-60 cells vs. HL-60 + ConA cells based on C_{sm}. These results indicate that C_{sm} is sensitive to both CD and ConA treatments of cells and can be effectively used for cell type classification.

In addition, in comparison to the cell type classification based on μ_{cy} only, when two or three intrinsic parameters were used in combination, significantly higher success rates were obtained. For the classification of HL-60 cells with and without CD treatments, the classification rate based on σ_{cy} and C_{sm} (83.4%) was higher than the classification rates based on σ_{cy} (81.1%) or C_{sm} (80.1%) only, which further validated the observation that CD treatment can produce differences in both membrane and cytosolic portions. As to the classification of HL-60 cells with and without ConA treatments, the classification rate based on σ_{cy} and C_{sm} (75.6%) was marginally higher than the classification rate based on C_{sm} (72.5%) only, which further validated the observation that ConA treatment can only produce difference on cell membranes without significantly modulating cytosolic portions. Furthermore, the classification rates based on μ_{cy} and three parameters in combination were quantified as 59.6% vs. 88.0% for HL-60 cells vs. HL-60 + CD cells and 54.2% vs. 75.6% for HL-60 cells vs. HL-60 + ConA cells, which confirmed the importance of collecting multiple biophysical markers in cell type classification and cell status evaluation.

Furthermore, the microfluidic platform was used to quantify cytoplasmic viscosity, cytoplasmic conductivity and specific membrane capacitance of single granulocytes from healthy donors. Figure 4(a, b, c) shows scatter plots of μ_{cy} vs. R_c, box and distribution plots of μ_{cy} for donor I and II. Specifically, three quartile values and peaking ranges of μ_{cy} of these granulocytes were quantified as 9.5 vs. 10.4 Pa•s, 15.6 vs. 17.2 Pa•s, 24.6 vs. 27.8 Pa•s and 10.5–16.8 vs. 16.8–26.8 Pa•s ($n_{cell} = 406$ of donor I vs. $n_{cell} = 458$ of donor II). In addition, the success rate of cell type classification based on μ_{cy} was quantified as 53.8% for donor I vs. donor II. Comparable values of μ_{cy} for donor I and II and the low success rate of cell-type classification between donor I and donor II suggest that there may exist a range of μ_{cy} for normal granulocytes (e.g., 10–20 Pa•s).
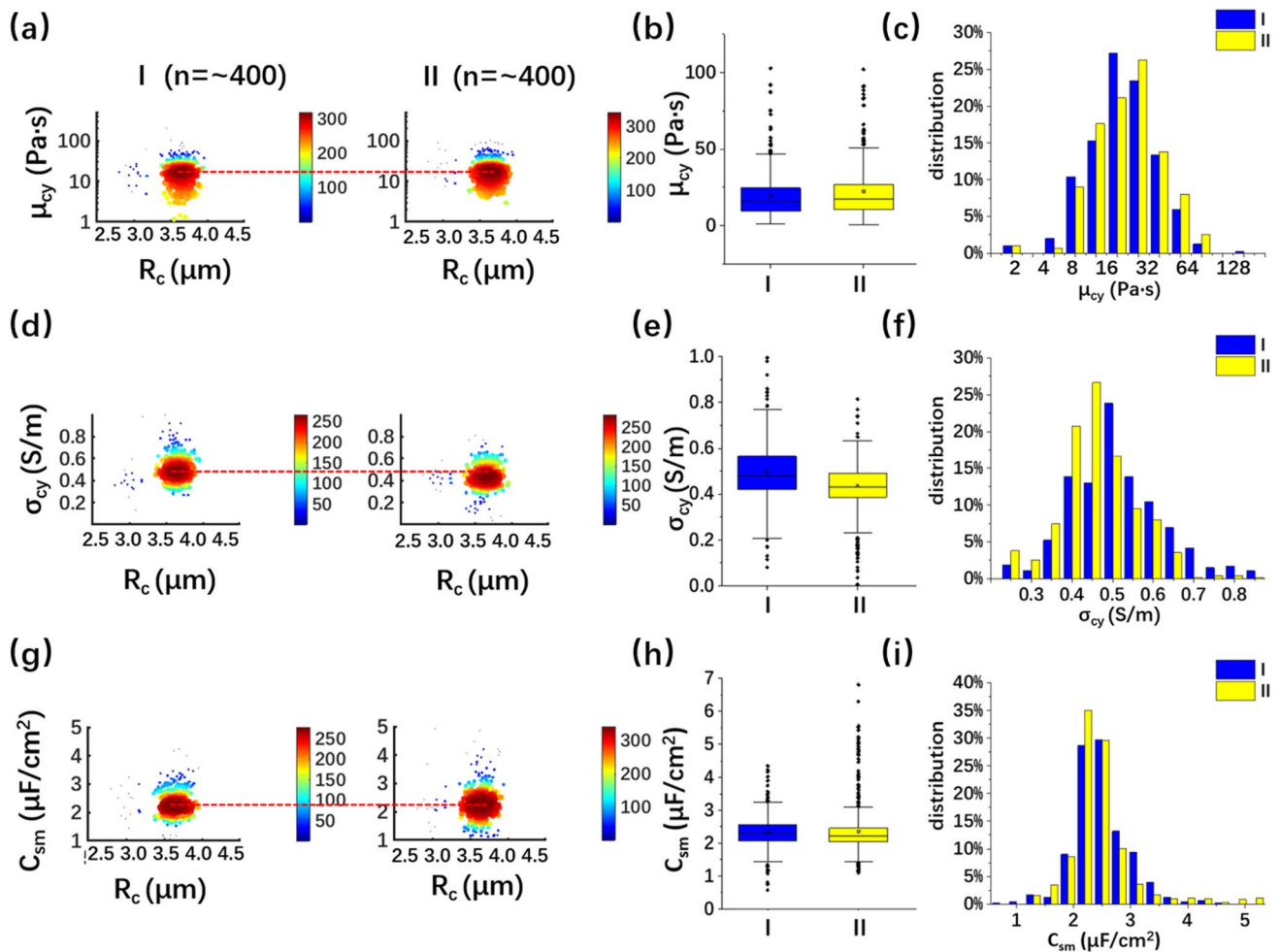
Fig. 4 **a**, **b**, **c** Scatter plots of μ_{cy} vs. R_c (**a**), box (**b**) and distribution plots (**c**) of μ_{cy} for granulocytes of Donor I and II; **d**, **e**, **f**: Scatter plots of σ_{cy} vs. R_c (**d**), box (**e**) and distribution plots (**f**) of σ_{cy} for granulo-cytes of Donor I and II. **g**, **h**, **i**: Scatter plots of C_{sm} vs. R_c (**g**), box (**h**) and distribution plots (**i**) of C_{sm} for granulocytes of Donor I and II

Figure 4(d, e, f) shows scatter plots of σ_{cy} vs. R_c, box and distribution plots of σ_{cy} for donor I and II. Specifically, three quartile values and peaking ranges of σ_{cy} of these granulocytes were quantified as 0.42 vs. 0.38 S/m, 0.49 vs. 0.43 S/m, 0.58 vs. 0.53 S/m and 0.45–0.50 vs. 0.40–0.45 S/m ($n_{cell} = 406$ of donor I vs. $n_{cell} = 458$ of donor II). In addition, the success rate of cell type classification based on σ_{cy} was quantified as 55.3% for donor I vs. donor II. Comparable values of σ_{cy} for donor I and II and the low success rate of cell type classification between donor I and donor II suggest that there may exist a range of σ_{cy} for normal granulocytes (e.g., 0.4–0.6 S/m).

Figure 4(g, f, i) shows scatter plots of C_{sm} vs. R_c, box and distribution plots of C_{sm} for donor I and II. Specifically, three quartile values and peaking ranges of C_{sm} of these granulocytes were quantified as 2.06 vs. 2.01 $\mu F/cm^2$, 2.25 vs. 2.25 $\mu F/cm^2$, 2.55 vs. 2.52 $\mu F/cm^2$ and 2.20–2.50 vs. 1.90–2.20 $\mu F/cm^2$ ($n_{cell} = 406$ of donor I vs. $n_{cell} = 458$ of donor II). In

addition, the success rate of cell type classification based on C_{sm} was quantified as 53.8% for donor I vs. donor II. Comparable values of C_{sm} for donor I and II and the low success rate of cell type classification between donor I and donor II suggest that there may exist a range of C_{sm} for normal granulocytes (e.g., 2.0–3.0 $\mu F/cm^2$).

In summary, the microfluidic platform developed in this study was demonstrated to characterize cytoplasmic viscosity, cytoplasmic conductivity and specific membrane capacitance from hundreds of single cells simultaneously. Based on these intrinsic biophysical markers, (1) successful classifications of HL-60 vs. HL-60 + CD cells with compromised cytoskeletons and HL-60 vs. HL-60 + ConA with membrane glycoproteins bound were realized; (2) estimated ranges including 10–20 Pa•s for μ_{cy}, 0.4–0.6 S/m for σ_{cy} and 2.0–3.0 $\mu F/cm^2$ for C_{sm} of normal granulocytes were obtained. From the perspective of technical developments, future studies may focus on the measurements of more

biophysical parameters (e.g., cortical tension and transmembrane potential) at the single-cell level to further improve the success rates of cell type classification. As to applications, this microfluidic platform can be further used to test more samples of white blood cells from both patients and benign counterparts to evaluate the potential in disease diagnosis at a label-free manner.

Data availability Cytoplasmic viscosity, cytoplasmic conductivity and specific membrane capacitance collected during this study are available as a supplementary file "Data of Single Cells". The Excel-based file is composed of five sheets named after five experimental groups which are HL-60, HL-60+CD, HL-60+ConA, Healthy Donor 1 and Healthy Donor 2, respectively. In each sheet, there are four columns which are cell number (column A), cytoplasmic viscosity (column B), cytoplasmic conductivity (column C) and specific membrane capacitance (column D).

References

Ahmmed SM et al (2018) Multi-sample deformability cytometry of cancer cells. APL Bioeng 2(3):032002–032002

Ahuja K et al (2019) Toward point-of-care assessment of patient response: a portable tool for rapidly assessing cancer drug efficacy using multifrequency impedance cytometry and supervised machine learning. Microsyst Nanoeng 5:34

Armistead FJ, Gala De Pablo J, Gadelha H, Peyman SA, Evans SD (2019) Cells under stress: an inertial-shear microfluidic determination of cell behavior. Biophys J 116:1127–1135

Bashant KR et al (2019) Real-time deformability cytometry reveals sequential contraction and expansion during neutrophil priming. J Leukoc Biol 105(6):1143–1153

Becker FF, Wang XB, Huang Y, Pethig R, Vykoukal J, Gascoyne PRC (1995) Separation of human breast-cancer cells from blood by differential dielectric affinity. Proc Natl Acad Sci USA 92(3):860–864

Che J, Yu V, Garon EB, Goldman JW, Di Carlo D (2017) Biophysical isolation and identification of circulating tumor cells. Lab Chip 17(8):1452–1461

Cross SE, Jin YS, Rao J, Gimzewski JK (2007) Nanomechanical analysis of cells from cancer patients. Nat Nanotechnol 2(12):780–783

Darling EM, Carlo DD (2015) High-throughput assessment of cellular mechanical properties. Annu Rev Biomed Eng 17(1):35–62

Davidson PM et al (2019) High-throughput microfluidic micropipette aspiration device to probe time-scale dependent nuclear mechanics in intact cells. Lab Chip 19(21):3652–3663

De Ninno A et al (2019) High-throughput label-free characterization of viable, necrotic and apoptotic human lymphoma cells in a coplanar-electrode microfluidic impedance chip. Biosens Bioelectron 15:111887

Deng Y et al (2017) Inertial microfluidic cell stretcher (iMCS): fully automated, high-throughput, and near real-time cell mechanotyping. Small 13:1700705

Fan W, Chen X, Ge Y, Jin Y, Jin Q, Zhao J (2019) Single-cell impedance analysis of osteogenic differentiation by droplet-based microfluidics. Biosens Bioelectron 145:111730

Feng Y, Huang L, Zhao P, Liang F, Wang W (2019) A microfluidic device integrating impedance flow cytometry and electric impedance spectroscopy for high-efficiency single-cell electrical property measurement. Anal Chem 91(23):15204–15212

Fregin B et al (2019) High-throughput single-cell rheology in complex samples by dynamic real-time deformability cytometry. Nat Commun 10(1):415

Guruprasad P et al (2019) Integrated automated particle tracking microfluidic enables high-throughput cell deformability cytometry for red cell disorders. Am J Hematol 94(2):189–199

Hassan U et al (2017) A point-of-care microfluidic biochip for quantification of CD64 expression from whole blood for sepsis stratification. Nature Commun 8:15949

Honrado C, Ciuffreda L, Spencer D, Ranford-Cartwright L, Morgan H (2018) Dielectric characterization of *Plasmodium falciparum*-infected red blood cells using microfluidic impedance cytometry. J R Soc Interf. https://doi.org/10.1098/rsif.2018.0416

Jacobi A, Rosendahl P, Krater M, Urbanska M, Herbig M, Guck J (2019) Analysis of biomechanical properties of hematopoietic stem and progenitor cells using real-time fluorescence and deformability cytometry. Methods Mol Biol 2017:135–148

Jaffe A, Voldman J (2018) Multi-frequency dielectrophoretic characterization of single cells. Microsyst Nanoeng 4:23–23

Kang JH et al (2019) Noninvasive monitoring of single-cell mechanics by acoustic scattering. Nat Methods 16(3):263–269

Leblanc-Hotte A et al (2019) On-chip refractive index cytometry for whole-cell deformability discrimination. Lab Chip 19(3):464–474

Liang H, Tan H, Chen D, Wang J, Chen J, Wu M-H (2019) Single-cell impedance flow cytometry. In: Santra TS, Tseng F-G (eds) Handbook of single cell technologies. Springer, Singapore, pp 1–31

Liu J, Qiang Y, Alvarez O, Du E (2018) "Electrical impedance microflow cytometry with oxygen control for detection of sickle cells. Sens Actuators B 255(Pt 2):2392–2398

MATLAB (2016). https://www.mathworks.com/

Nyberg KD, Hu KH, Kleinman SH, Khismatullin DB, Butte MJ, Rowat AC (2017) Quantitative deformability cytometry: rapid, calibrated measurements of cell mechanical properties. Biophys J 113(7):1574–1584

Prieto JL et al (2016) Monitoring sepsis using electrical cell profiling. Lab Chip 16(22):4333–4340

Reale R, De Ninno A, Businaro L, Bisegna P, Caselli F (2019) High-throughput electrical position detection of single flowing particles/cells with non-spherical shape. Lab Chip 19(10):1818–1827

Reichel F, Mauer J, Nawaz AA, Gompper G, Guck J, Fedosov DA (2019) High-throughput microfluidic characterization of erythrocyte shapes and mechanical variability. Biophys J 117(1):14–24

Ren X, Ghassemi P, Strobl JS, Agah M (2019) Biophysical phenotyping of cells via impedance spectroscopy in parallel cyclic deformability channels. Biomicrofluidics 13(4):044103

Rosendahl P et al (2018) Real-time fluorescence and deformability cytometry. Nat Methods 15:355

Serhatlioglu M, Asghari M, Tahsin GM, Elbuken C (2019) Impedance-based viscoelastic flow cytometry. Electrophoresis 40(6):906–913

Toepfner N et al (2018) Detection of human disease conditions by single-cell morpho-rheological phenotyping of blood. Elife. https://doi.org/10.7554/eLife.29213

Wang H, Sobahi N, Han A (2017) Impedance spectroscopy-based cell/particle position detection in microfluidic systems. Lab Chip 17(7):1264–1269

Wang K et al (2017) Specific membrane capacitance, cytoplasm conductivity and instantaneous Young's modulus of single tumour cells. Sci Data 4:170015

Wang K et al (2019) Microfluidic cytometry for high-throughput characterization of single cell cytoplasmic viscosity using crossing constriction channels. Cytometry A. https://doi.org/10.1002/cyto.a.23921

Wu PH et al (2018) A comparison of methods to assess cell mechanical properties. Nat Methods 15(7):491–498

Xavier M et al (2016) Mechanical phenotyping of primary human skeletal stem cells in heterogenous populations by real-time deformability cytometry. Integr Biol 8(5):616–623

Xavier M, de Andres MC, Spencer D, Oreffo ROC, Morgan H (2017) Size and dielectric properties of skeletal stem cells change critically after enrichment and expansion from human bone marrow: consequences for microfluidic cell sorting. J R Soc Interf 14:133

Xu Y, Xie X, Duan Y, Wang L, Cheng Z, Cheng J (2016) A review of impedance measurements of whole cells. Biosens Bioelectron 77:824–836

Yang D, Ai Y (2019) Microfluidic impedance cytometry device with N-shaped electrodes for lateral position measurement of single cells/particles. Lab Chip 19(21):3609–3617

Yang X, Chen Z, Miao J, Cui L, Guan W (2017) High-throughput and label-free parasitemia quantification and stage differentiation for malaria-infected red blood cells. Biosens Bioelectron 98:408–414

Yang D, Zhou Y, Zhou Y, Han J, Ai Y (2019) Biophysical phenotyping of single cells using a differential multiconstriction microfluidic device with self-aligned 3D electrodes. Biosens Bioelectron 133:16–23

Zhang Y et al (2019) Crossing constriction channel-based microfluidic cytometry capable of electrically phenotyping large populations of single cells. Analyst 144(3):1008–1015

Zhao Y et al (2018) Development of microfluidic impedance cytometry enabling the quantification of specific membrane capacitance and cytoplasm conductivity from 100,000 single cells. Biosens Bioelectron 111:138–143

Zheng Y, Nguyen J, Wei Y, Sun Y (2013) Recent advances in microfluidic techniques for single-cell biophysical characterization. Lab Chip 13(13):2464–2483

Zhou Y, Basu S, Laue E, Seshia AA (2016) Single cell studies of mouse embryonic stem cell (mESC) differentiation by electrical impedance measurements in a microfluidic device. Biosens Bioelectron 81:249–258

Zhou Y, Yang D, Zhou Y, Khoo BL, Han J, Ai Y (2018) Characterizing deformability and electrical impedance of cancer cells in a microfluidic device. Anal Chem 90(1):912–919

Publisher's Note Springer Nature remains neutral with regard to jurisdictional claims in published maps and institutional affiliations.